Journal of Manufacturing Processes 75 (2022) 514–526

Contents lists available at ScienceDirect

Journal of Manufacturing Processes

journal homepage: www.elsevier.com/locate/manpro

Investigation on machinability in turning of as-cast and T6 heat-treated Al-(3, 7, 12%)Si-0.6%Mg alloys

Pedro Augusto Bottlender Machado [a], José Maria do Vale Quaresma [b], Amauri Garcia [c], Carlos Alexandre dos Santos [a,*]

[a] Pontifícia Universidade Católica do Rio Grande do Sul - PUCRS, School of Technology, 6681 Ipiranga Ave., 90619-900 Porto Alegre, RS, Brazil
[b] Universidade Federal do Pará - UFPA, Institute of Technology, 01 Augusto Correa St., 66075-110 Belém, PA, Brazil
[c] Universidade de Campinas - UNICAMP, Department of Manufacturing and Materials Engineering, 13083-860 Campinas, SP, Brazil

ARTICLE INFO

Keywords:
Al-Si-Mg alloys
Machinability
Solidification
Heat treatment
Microstructure
Hardness

ABSTRACT

The machinability in turning of Al-Si-Mg alloys under as-cast and heat-treated conditions has been investigated. Three alloys with 3%, 7% and 12%Si and 0.6%Mg contents (wt%) were prepared. Unsteady solidified ingots were obtained in a vertical upward directional solidification apparatus using an instrumented cylindrical water-cooled mold. Samples extracted from the ingots were characterized by scanning electron microscopy (SEM) and energy dispersive spectroscopy (EDS) examinations and by Brinell hardness tests, before and after T6 heat treatments (540 °C solutioning temperature for 10 h, water quenching at 25 °C and artificial aging at 155 °C for 5 h). Specimens in both the as-cast and heat-treated conditions were subjected to machinability tests as a function of cutting force in face turning operation using a CNC lathe machine, fixing parameters as cutting depth, feed rate, cutting speed, and cutting tool. The as-cast microstructure consists of a dendritic α-Al rich phase and an interdendritic eutectic microconstituent (α-Al + Si particles). As the alloy Si content increased, the solidification cooling rate increased, the amount and size of α-Al dendrites decreased while the amount of eutectic mixture increased. After heat treatment, Si particles were found to be more rounded and an increase in fraction of Mg_2Si was observed. The hardness profile declines along the length of the as-cast ingots, however the values improved with both alloy Si content and heat treatment. The as-cast alloys showed maximum cutting force at the beginning of the process, decreasing during machining progress, whereas in the heat-treated condition the cutting forces showed values almost constant. The results suggest a more stable machinability behavior during turning of the heat-treated alloys as a consequence of a more homogenous microstructure and hardness.

1. Introduction

Binary Al-Si alloys are the most important and widely used of all aluminum alloys in the as-cast condition due to their excellent castability, low thermal expansion, low-cost production, moderate mechanical strength, and high wear resistance [1–4]. Gravity casting (permanent mold casting, green or dry sand casting, investment casting) and low-pressure die casting processes are used to manufacture a variety of parts and components. These alloys are an attractive option for applications in the metalworking and automotive industries to produce components such as pistons, engine blocks, pumps, rods, wheels, gears [5–9]. In the aeronautical and aerospace industries, they are used in non-structural components, especially in mechanical and hydraulic systems, for example, valve housings, turbine impellers, cooling fans, clamps, rollers, pulleys, sticks, manifolds [10–12]. In general, the microstructure of hypoeutectic alloys consists of an α-Al rich matrix and a eutectic microconstituent (α-Al + Si phases). With Mg addition, the as-cast microstructure is composed of the α-Al matrix, the eutectic mixture and the Mg_2Si phase. In the presence of impurities such as Fe, complex intermetallic compounds can be formed [13]. Depending on the magnitude of the solidification cooling rate, the α-Al matrix can show either cellular (under higher cooling rates) or dendritic (under lower cooling rates) morphologies. In addition, higher cooling rates also induce increase in the amount of Mg_2Si particles. An opposite behavior is observed in the formation of Fe intermetallic which increases with decreasing cooling rate [14–15]. The presence of both Si and Mg enables the ternary Al-Si-Mg alloys to be heat-treated by precipitation hardening due to the controlled formation of Mg_2Si intermetallic particles,

* Corresponding author.
E-mail address: carlos.santos@pucrs.br (C.A. dos Santos).

https://doi.org/10.1016/j.jmapro.2022.01.028
Received 1 September 2021; Received in revised form 9 December 2021; Accepted 9 January 2022
Available online 21 January 2022

improving mechanical properties as hardness, tensile strength, and fatigue resistance [16–18], as well as electrical, wear and corrosion responses [19–21]. Among the commercial Al-Si-Mg alloys, according to the Aluminum Association, the AA 356.0 (6.5–7.5%Si - 0.20-0.45%Mg - 0.6%Fe) and the AA 357.0 (6.5–7.5%Si - 0.45-0.60%Mg - 0.15%Fe) alloys are extensively used in the foundry industry, in both as-cast and heat-treated conditions [22–24].

Since the main properties of alloys are directly linked to their microstructure features, it is fundamental to understand the influence of these characteristics on the machinability, the ease with which the alloy can be cut. The influence of aspects as manufacturing processes and machining operational parameters are frequently related to the machinability performance of ferrous [25–26] and non-ferrous alloys [27–28]. As reported in recent reviews [29–30], aluminum alloys generally display good machinability when compared to steels. However, higher cutting force, cutting temperature and surface roughness can be observed in the case of pure aluminum or soft aluminum alloys due to their higher ductility. In order to minimize these problems, strategies for selecting the appropriate cutting tool, improving operational parameters, increasing alloys hardness and strength, adding free-cutting elements, and using cooled or dry conditions, are the most recommended practices. In the case of wrought aluminum alloys, as AA6061, 6351, 6013 and 2117, the influence of microstructural features, machining parameters and heat treatments on alloys machinability considering parameters such as cutting forces, surface roughness, tool life, and tool wear rate have been reported by Froehlich [31], Veera ajay [32], Gonçalves [33], and Akyuz [34]. In the as-cast condition, Bayraktar and Afyon [35] investigated the machinability of an Al-7Si alloy with Zn and Cu additions under dry drilling process in a CNC vertical machining center. Operational parameters as cutting depth, feed rate and cutting speed were kept constant and an uncoated carbide drill was used as cutting tool. They observed that the increase in hardness and strength of the alloys due to Zn and Cu additions decreased the cutting force, torque, and surface roughness. Barzani et al. [36] have investigated how Bi, Sb and Sr additions affect microstructure formation and machining response in a commercial Al-Si-Cu alloy. Turning machining tests were performed under dry condition, and speed cutting and feed rate variations. The results showed that the additions of Bi, Sb and Sr modified the morphology of Si particles. As a consequence, a softer matrix was obtained, the tendency of build-up edge formation was enlarged, and the cutting force increased, mainly with Sr and Sb additions. An exception was noted with the Bi-containing alloy, which displayed the lowest cutting force compared with the other alloys. Kishawy et al. [37] investigated the effect of cooling condition on the machinability of the A356 alloy under high-speed face milling machining. Characteristics as tool wear, chip morphology and surface roughness were analyzed. It was observed that the main wear mechanism was abrasion due to the presence of hard Si particles. The best cooling condition was achieved using MQL (minimum quality of lubricant) with 5200 m/min cutting speed and uncoated carbide insert, demonstrating the feasibility of the process. The influence of the precipitation hardening heat treatment on the machinability of A359 and A319 alloys was performed by Tash et al. [38]. The results showed that the cutting force increased with the increase in hardness as a consequence of the formation of Al_2Cu and Mg_2Si precipitates in the matrix.

Despite the aforementioned works, few studies have reported the effect of microstructural formation as a function of solidification/heat treatment conditions and the resulting mechanical properties on the machinability of Al-Si-Mg alloys. In this view, the present work aims to investigate the effects of alloy Si content (3, 7 and 12 wt%), solidification conditions and precipitation hardening heat treatment on microstructure features, hardness, and machinability of three Al-Si-Mg alloys.

2. Experimental procedure

For the experimental investigation, three Al-Si-Mg alloys were prepared using silicon carbide crucibles covered with boron nitride in an electric resistance pit furnace for melting small blocks of commercial eutectic aluminum-silicon alloy (Al-11.9wt%Si), pure aluminum (99.9% purity) and pure magnesium (99.9% purity). The chemical composition of the alloys analyzed by optical emission spectrometry (average values of five measurements in each sample) is presented in Table 1. The amounts of Si and Mg are close to the required values, and the presence of Fe was observed in all alloys. With a view to determining the *Liquidus* (T_L) and *Solidus* (T_S) temperatures of each alloy, thermal analyzes were performed to acquire cooling curves during solidification under high cooling rates. The alloys were poured into a cylindrical SAE 1010 steel mold (30 mm × ϕ50 mm) with a type-K thermocouple located at the cavity center, and the obtained cooling curves are shown in Fig. 1. The temperatures corresponding to the solidification range for the Al3Si0.6Mg alloy were determined to be $T_L = 621$ °C and $T_S = 529$ °C, the Al7Si0.6Mg alloy had the experimental values of $T_L = 601$ °C and $T_S = 550$ °C, while the Al12Si0.6Mg alloy showed values close to those of the eutectic alloy, i.e., $T_L = 567$ °C and $T_S = 564$ °C. The time-scale axis was suppressed and expressed as an arbitrary unit (a.u.) to permit plotting all curves in the same graph.

The casting assembly used in the directional solidification experiments is shown in Fig. 2a. The alloys were melted in-situ in an AISI 1020 carbon steel mold, and type-K thermocouples (1.6 mm-diameter) were used to measure the temperatures in the casting during solidification. The bottom part of the mold was closed with a 5-mm thick steel sheet. Details about the solidification apparatus can be found in previous works [39–40]. Each alloy was melted with a superheat of about 10% above the *Liquidus* temperature assessed in Fig. 1. When the desired melting temperature was attained, water at a flow-rate of 4 l/min was initiated at the bottom of the mold. The cooling curves acquired by the six thermocouples strategically positioned at specific locations along the height of the mold cavity from the cooled bottom (TC1–6 mm, TC2–12 mm, TC3–18 mm, TC4–24 mm, TC5–30 mm, TC6–50 mm) were used to determine the tip growth rate (V_L), the liquid thermal gradient (G_L) and the liquid cooling rate ($\dot{T}$). The time-derivative of the cooling curves (dT/dt) immediately ahead the *Liquidus* temperature at each thermocouple position (P) permitted the evolution of $\dot{T}$ to be determined along the length of the ingots; V_L was obtained by the time-derivative of experimental functions $P = f(t_L)$, where t_L is the time of passage of the *Liquidus* isotherm by each thermocouple, and $G_L = \dot{T}/V_L$. The experiments were repeated with identical parameters to obtain two ingots of each alloy.

The metallography of longitudinal samples extracted from the center of the ingots (Fig. 2b) was performed along with scanning electron microscopy (SEM) and energy dispersive X-ray spectroscopy (EDS). Traditional metallographic techniques were used by grinding, polishing and etching using a HF 5% solution. The secondary dendrite arm spacings (λ_2) were measured from the bottom to the top of the ingots. At least 30 measurements were taken for each selected position. Brinell hardness tests were carried out on both faces of the longitudinal samples (three measurements were performed on each sample taken at 12, 30 and 50 mm from the cooled bottom of each ingot, corresponding to the thermocouples TC2, TC5 and TC6, respectively), according to the ASTM E 10 Standard Test Method [41], using a test load of 2500 N, a 5 mm-diameter sphere and a dwell time of 30 s. Precipitation hardening heat treatments were carried out at 540 °C ± 3 °C for 10 h into a resistance muffle furnace for solutioning, quenched into water at 25 °C ± 2 °C, followed by artificial aging at 155 °C ± 3 °C for 5 h.

Table 1
Chemical composition of the alloys (wt%).

Alloys	Al	Si	Mg	Fe	Other
Al3Si0.6Mg	Balance	2.98	0.62	0.15	0.011
Al7Si0.6Mg	Balance	7.16	0.65	0.20	0.011
Al12Si0.6Mg	Balance	12.33	0.54	0.22	0.051

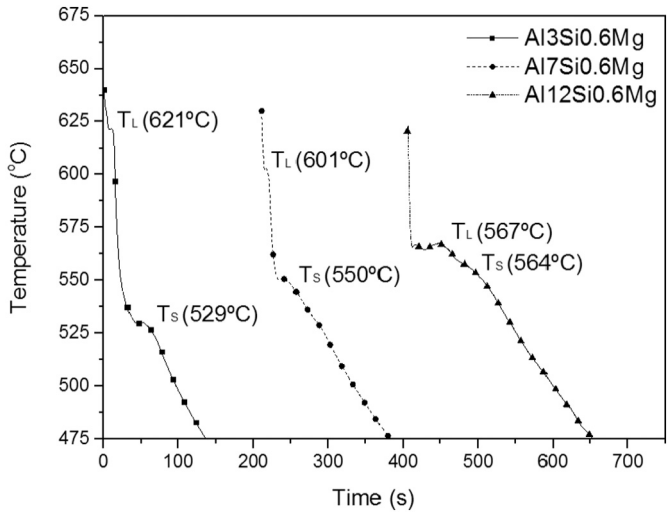

Fig. 1. Cooling curves of the alloys obtained by thermal analysis.

The machinability evaluation was performed in face turning operation as a function of the cutting force, using a conventional CNC lathe (*Mazak*, *Quick Turn Nexus 100-II model*) and cutting inserts of TiN cemented carbide (*Iscar*, *VCGT 160408-AS*). According to the manufacturer's specifications, the recommended cutting speed ranges from 60 m/min to 1500 m/min. Considering a minimum sample diameter of 20 mm and a cutting speed of 250 m/min, the determined rotation is 3980 rpm, which is suitable since the maximum rotation of the CNC lathe is 6000 rpm. Also, the cutting depth should vary between 0.5 mm and 3.0 mm for aluminum alloys. Since the cutting depth must be less than the tool nose radius for tuning process, in the present case the cutting depth must be less than 0.8 mm. Finally, the recommended feed rate is between 0.10 mm/rev to 0.25 mm/rev, and an intermediate value was chosen. Then, the cutting depth, feed rate and cutting speed, with values of 0.5 mm, 0.15 m/rev and 250 m/min, respectively, were selected and kept constants during all machining tests, minimizing the effect of machining parameters on cutting forces and focusing on the influences of microstructure and hardness on machinability. A three-component force dynamometer (Kistler, 9441B *model*) mounted on the turret/tool holder adapter (Fig. 2c) was used for measuring the cutting forces. The ingot was divided in three 3 regions: 0–20 mm, 20–40 mm and 40–60 mm from the cooled bottom, in order to associate the cutting force with each thermocouple position (TC2, TC5 and TC6). New inserts were used for each region. In order to avoid overspeed at the center of the ingot, a central hole with 20 mm diameter was drilled in the ingot. Since the speed cutting was kept constant, the spindle rotational speed started at 750 rpm at the external diameter (100 mm) and achieved at 4000 rpm at the final diameter (20 mm).

3. Results and discussion

The as-cast microstructures revealed by SEM images at 30 mm from the bottom of the ingots (corresponding at the location of the thermocouple TC5) are shown in Fig. 3. EDS analyses were used to identify phases and precipitates. For the Al3Si0.6Mg alloy (Fig. 3a), a typical microstructure consisting of a dendritic α-Al rich matrix (gray phase – spectrum #1) and an interdendritic (α-Al + Si particles) eutectic mixture (Chinese-script like structure – spectrums #2 and #3) was observed. Since the concentration of dissolved solutes in the α-Al matrix is small, their peaks were undetected in EDS analysis. Few globular particles with the presence of Al, Si, Mg and Fe were noted (spectrums #4 and #5), as shown in detail in Fig. 3a. These rounded particles are probably the ternary α-Al + Si + Mg_2Si eutectic microconstituent [42]. The microstructure of the Al7Si0.6Mg alloy is composed by the dendritic α-Al phase (spectrum #1), a higher amount of the eutectic α-Al + Si mixture (spectrums #2 and #3), and globular precipitates dispersed along the matrix (spectrums #4 and #5), as depicted in Fig. 3b. The 12%Si-containing alloy showed a quasi-fully eutectic microstructure (α-Al + Si), as seen in Fig. 3c. Some needle-like Fe-rich phases were observed in all alloys samples as a function of Fe-content, as well as the presence of Fe in the eutectic mixtures. As confirmed by Liu [13], Taylor [43] and Bidmeshki [44], the needle-shaped intermetallic compound is identified as the β-Al_5FeSi phase, which is formed after solidification of the α-Al matrix. According to the equilibrium pseudo-binary phase diagram of Al-2.4%Si-x%Mg alloys simulated by Zhu et al. [45], the solidification path of an Al-2.4%Si alloy with 0.6%Mg is: L → (L + α-Al) → (L + α-Al + Si) → (α-Al + Si) → (α-Al + Si + Mg_2Si), when considering the absence of Fe. Lima et al. [46] simulated a pseudo binary phase diagram under non-equilibrium conditions of the Al-7%Si-0.6%Mg alloy containing 0.15% Fe content and concluded that β-Al_5FeSi and π-$Al_8Mg_3FeSi_6$ intermetallics were present in the final as-cast microstructure. These results were confirmed by Silva et al. [42] on an Al-7Si-3Mg-0.15Fe alloy.

Using the cooling curves acquired during solidification (Fig. 4a to c), the tip growth rate (V_L), the liquid thermal gradient (G_L) and the tip cooling rate ($\dot{T}$) along the length of the ingots were determined, as shown in Fig. 4d to f. The temperature profiles of the Al3Si0.6Mg alloy (Fig. 4a) indicates that the Liquidus temperature was achieved faster for positions far from the bottom of the ingot when compared with the other alloys, while the Al12Si0.6Mg alloy (Fig. 4c) exhibited the longest time to the beginning of solidification.

Despite the aforementioned behavior, the Al12Si0.6Mg alloy casting exhibited the highest profile of $\dot{T}$ values (Fig. 4f) and the lowest profile of V_L (Fig. 4d). This is attributed to the influence of the thermal gradient profile, which is much higher for the Al12Si0.6Mg alloy casting as compared with those of the two other examined alloys (Fig. 4e). This is a consequence of the highest liquid metal superheat exhibited by the Al12Si0.6Mg alloy ingot, as evidenced in Fig. 4c.

Fig. 5a shows the longitudinal macrostructures and microstructures obtained from a set of samples extracted along the length of the solidified ingots. Columnar macrostructures were observed along the entire casting length, and insignificant variances were observed in terms of grain size. The evolution of the secondary dendrite arm spacing (λ_2) as a function of the solidification cooling rate ($\dot{T}$) is shown in Fig. 5b. In the present work, it was observed that λ_2 decreases with the increase in the alloy Si content. In the experimentally derived growth laws $\lambda_2 = f(\dot{T})$, different exponents were obtained for each alloy, varying from 0.18 to 0.34. In general, the literature has reported values close to 0.33 for Al-Si-Mg alloys [47–48].

Fig. 6 shows the results of Brinell hardness measurements carried out in samples extracted at 12, 30 and 50 mm from the cooled bottom of the ingots for both as-cast and heat-treated conditions. In general, the hardness increases as the alloy Si content increases in both conditions, which is associated to the increase in the amount of the eutectic microconstituent. When analyzing the variation in hardness along the length of the ingots, a slight decrease can be noted in the as-cast condition (Fig. 6a) with increasing distance from the cooled bottom, whereas the hardness values in the heat-treated ingots are almost constant. In addition, it was noted a substantial increase in hardness (approximately 1.6× higher) from the as-cast samples to those heat-treated. This behavior is due to the Mg_2Si precipitation during the artificial aging procedure. The results are similar to those reported by Yildirim et al. [16] for an A356-base alloy (Al-7%Si-0.3Fe) with Mg additions of 0.43, 0.67 and 0.86 wt%, subjected to the T6 heat treatment. Kaleel [19] found smaller hardness responses with an Al-7%Si-0.3%Mg alloy subjected to different solutioning and artificial aging conditions (temperature and time) probably due to the smaller amount of Mg in that alloy. In order to correlate the hardness with a representative microstructure feature, a Hall-Petch type relation was obtained, given by $HB = a + b * (\lambda_2)^{-0.5}$, which permits estimating the Brinell

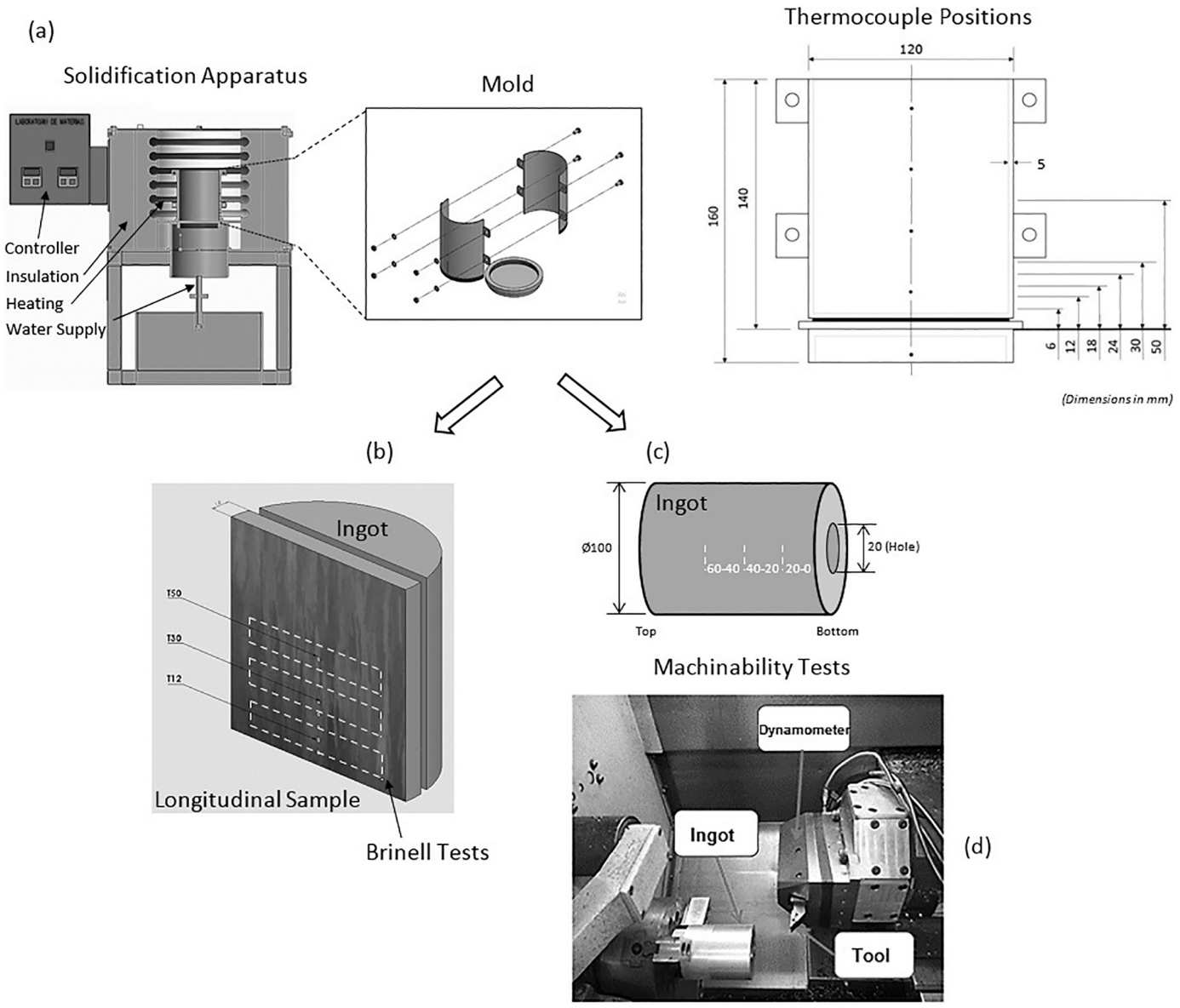

Fig. 2. (a) Representation of the solidification apparatus, (b) solidified ingot, (c) specimen extracted for mechanical tests, and (d) cylindrical ingot for machinability tests.

hardness as a function of the inverse square-root of λ_2 for the examined alloys, as shown in Fig. 6c.

Some typical microstructures obtained for the alloys after heat treatment are shown in Fig. 7. It can be seen that the eutectic Si particles, which were of an irregular faceted morphology in the as-cast condition, have been modified into more disconnected and rounded particles. Yao and Taylor [49] found similar microstructures for the Al-7Si-0.4 Mg-0.12Fe alloy after T6 heat treatment. As concluded by the authors, the heat-treated iron-containing phases are more refined than those of the as-cast condition. Costa et al. [50] reported the influence of the T6 heat treatment on the morphology and distribution of Si particles and λ_2 in an Al-Si-Cu alloy. According to the results, λ_2 tends to increase slightly after the T6 heat treatment in special for solution times higher than 5 h, which induces the progress of the coarsening process of λ_2. The authors reported that the morphology of Si particles modified to a mixture of fibers and spheroids after the T6 heat treatment. In a subsequent work, the T6 heat treatment applied in as-cast samples was reported not to affect λ_2 features [51]. However, more spheroidized Si particles were observed when smaller λ_2 values were obtained in the as-cast microstructure. When the alloy Si-content increased to 7%, the same behavior was observed, with spheroidized-like Si particles being predominant close to the bottom of the ingot [52].

The cutting forces obtained in the machining experiments are summarized in Fig. 8 as a function of position along the length of ingots in both as-cast and heat-treated conditions. When the as-cast alloys were machined, it is worth noting that all alloys showed maximum cutting force values at the beginning of each cutting operation, decreasing as the machining progresses. This can be attributed to the variation of microstructure and hardness of samples extracted from different regions along the length of the ingots (TC2: 0–20 mm; TC5: 20–40 mm; TC6: 40–60 mm) and the heating of the material, which leads to soften the work material [29,32]. For the Al3Si0.6Mg alloy, the cutting force values at the beginning of the turning process were about 65 N, 78 N and 90 N in the regions corresponding to the TC2, TC5 and TC6 positions, respectively, decreasing to approximately 20 N, 30 N and 40 N at the end of the turning. In all regions, the variation in the cutting force during the process was approximately 47 N, which indicates a similar softening of the alloys during cutting, regardless of the alloy hardness. This can be

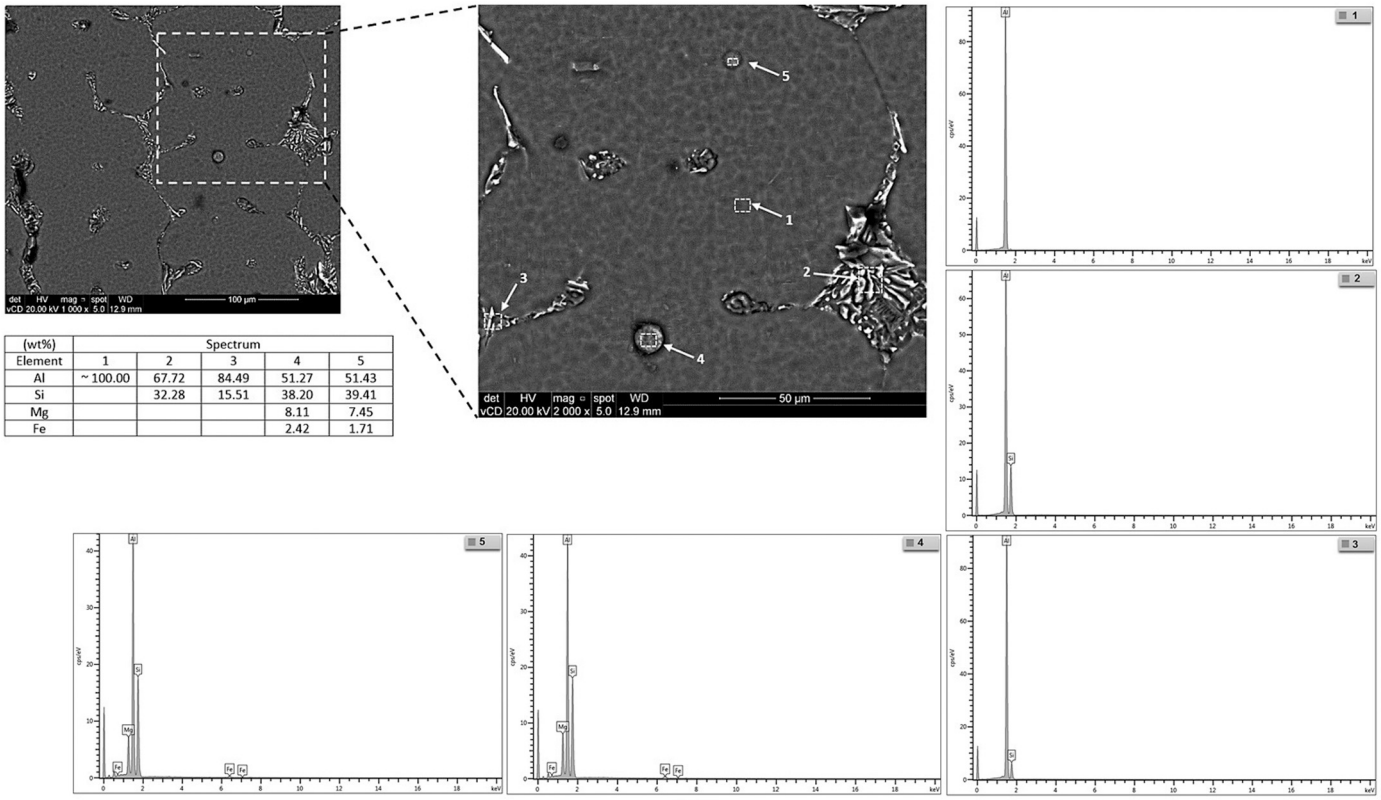

(wt%)	Spectrum				
Element	1	2	3	4	5
Al	~ 100.00	67.72	84.49	51.27	51.43
Si		32.28	15.51	38.20	39.41
Mg				8.11	7.45
Fe				2.42	1.71

(a)

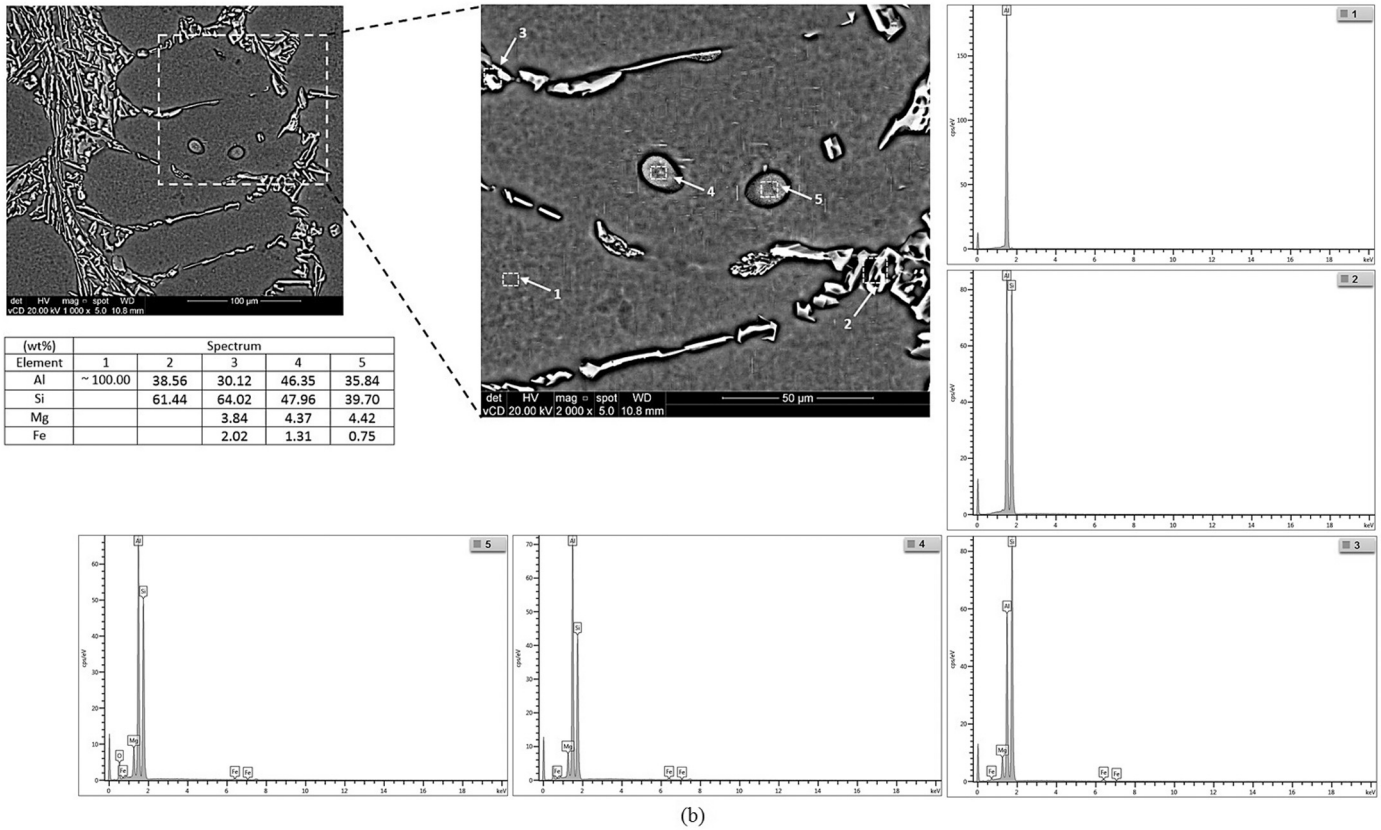

(wt%)	Spectrum				
Element	1	2	3	4	5
Al	~ 100.00	38.56	30.12	46.35	35.84
Si		61.44	64.02	47.96	39.70
Mg			3.84	4.37	4.42
Fe			2.02	1.31	0.75

(b)

Fig. 3. SEM micrographs and EDS analyses: (a) Al3Si0.6Mg, (b) Al7Si0.6Mg, (c) Al12Si0.6Mg alloys.

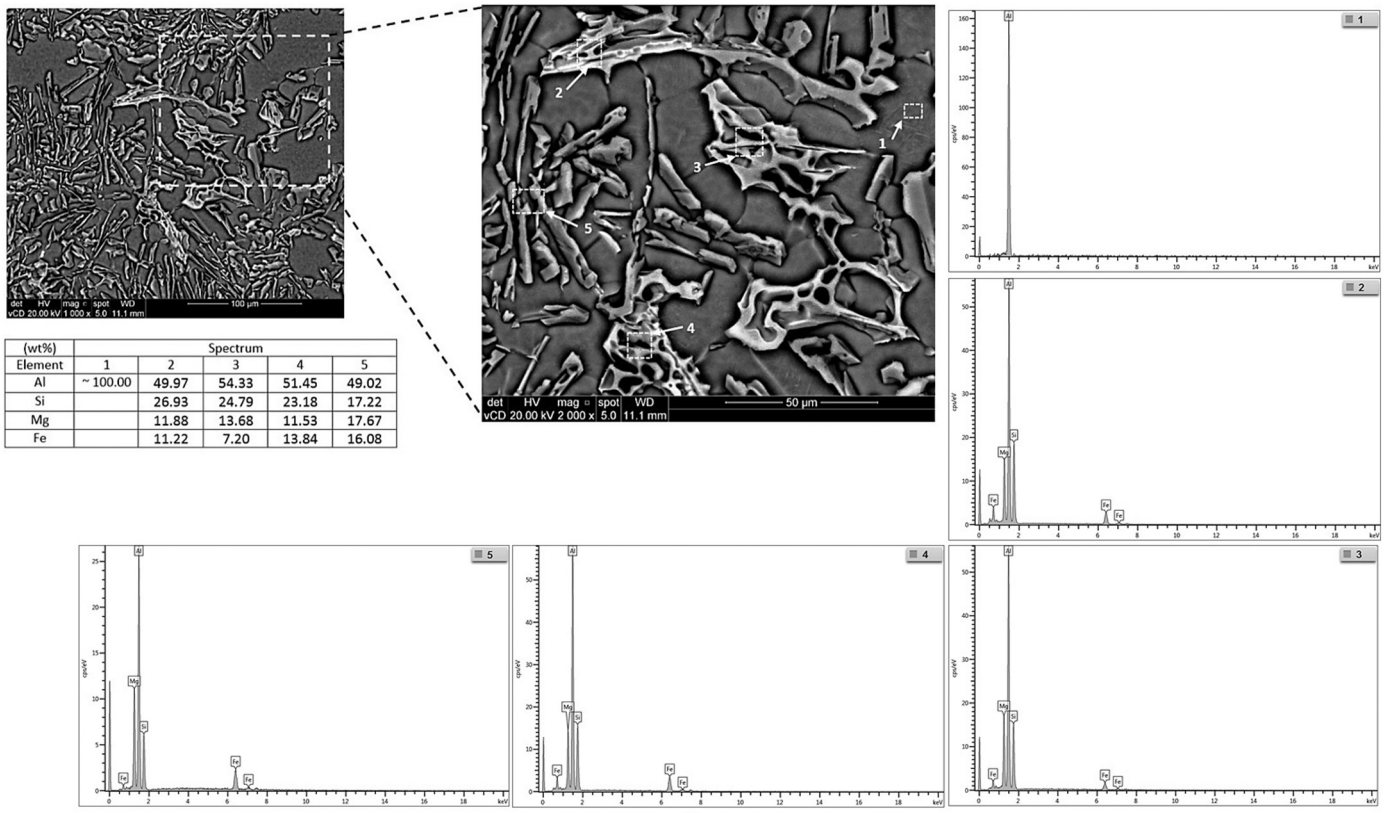

(wt%)	Spectrum				
Element	1	2	3	4	5
Al	~ 100.00	49.97	54.33	51.45	49.02
Si		26.93	24.79	23.18	17.22
Mg		11.88	13.68	11.53	17.67
Fe		11.22	7.20	13.84	16.08

(c)

Fig. 3. (*continued*).

associated with the characteristic of the microstructure, which consists predominantly of the α-Al rich matrix, a ductile and soft phase. With the increase in Si content from 3% to 7%, the cutting forces displayed variations in their behavior. The values at the beginning of cutting tend to decrease along with the positions at TC2 and TC5 regions, showing final cutting forces higher than those of the Al3Si0.6Mg alloy. The cutting force variations for the regions at TC2, TC5 and TC6 of the Al7Si0.6Mg alloy were about 25 N, 32 N and 50 N, respectively. While the smallest value observed at the position closest to the bottom of the ingot is related to the highest hardness and the more refined microstructure, the greatest variation obtained at the top of the ingot is linked to the smallest hardness and coarsest microstructure. According to Silva et al. [53] who investigated the influence of microstructure features on the machinability of an Al-7wt%Si cast alloy, the heating rate during machining increases with increasing secondary dendrite arm spacing (λ_2) and with increasing Si particle size, caused by increased efforts during machining. The authors concluded that the machinability decreased with microstructure refinement and hardness increase. The Al12Si0.6Mg alloy showed more stable values during machining, with the variation along the region decreasing slightly for all positions (65 N at the beginning and 45 N at the end of turning). This homogenous behavior occurred due to the hardness/microstructure conditions (higher hardness and higher amount of eutectic microconstituent), which require lower forces to remove the material. In the as-cast condition, it was evident that the high Si content induces the hardening of the alloy and the weakening of the chips, causing rupture of the removed material, and consequently, improving the machinability. This behavior was also reported by Kamiya et al. [54] in Al-Si casting alloys with Si contents ranging from 2% to 25%. As the Si content increased, the chips became shorter and fragmented as a result of the increase in the amount of eutectic Si microconstituent and the material hardness. Both conditions reduce material adhesion on the rake face of the tool, facilitating material removing. Akyuz [55] also observed increase in machinability with increasing Si content in hypoeutectic binary Al-Si casting alloys as the cutting force during turning decreased with increasing alloy Si content. When comparing the heat-treated and as-cast conditions, a significant change was observed for all alloys. The cutting forces showed constant values (approximately 55 N) independently of both alloy composition and position along the length of the ingot. This demonstrates that precipitation hardening has a beneficial effect on the machinability of the alloys, probably due to the tendency of embrittlement of the chips as a consequence of the increase in hardness [35]. However, Akyuz and Senaysoy [34] found opposite behavior in a comparison of cutting forces in turning of AA6013 alloy samples under unaged and aged conditions. The highest cutting forces were observed for the aged samples.

Fig. 9 shows images of chip formation and cutting tool surfaces after machining of the investigated alloys in both the as-cast and heat-treated conditions. As observed, chip formation changed depending on Si content and alloy condition. The chips were relatively longer and with a large radius of curvature in the alloy containing 3%Si, both in as-cast and heat-treated conditions. The chips became shorter and fragmented as the Si content increased to 7%. However, for the 12%Si alloy the chips were continuous and longer than for the 3%Si alloy, but the radius was smaller. When analyzing the cracks formed on the chip surfaces, it was observed that the incidence was more pronounced in the Al7Si0.6Mg alloy, followed by the Al3Si0.6Mg and Al12Si0.6Mg alloys, respectively. Build-up edge was observed on the rake face surface of the cutting tool after machining all alloys and conditions. The build-up edge was more severe for the alloy with 3%Si, and less severe for the 7%Si and 12%Si alloys. In general, build-up edge formation decreased with increasing Si content, probably due to the increase in alloy hardness as a function of the increase in the amount of the eutectic microconstituent and heat treatments, and consequent decrease in chip adhesion on the rake face of

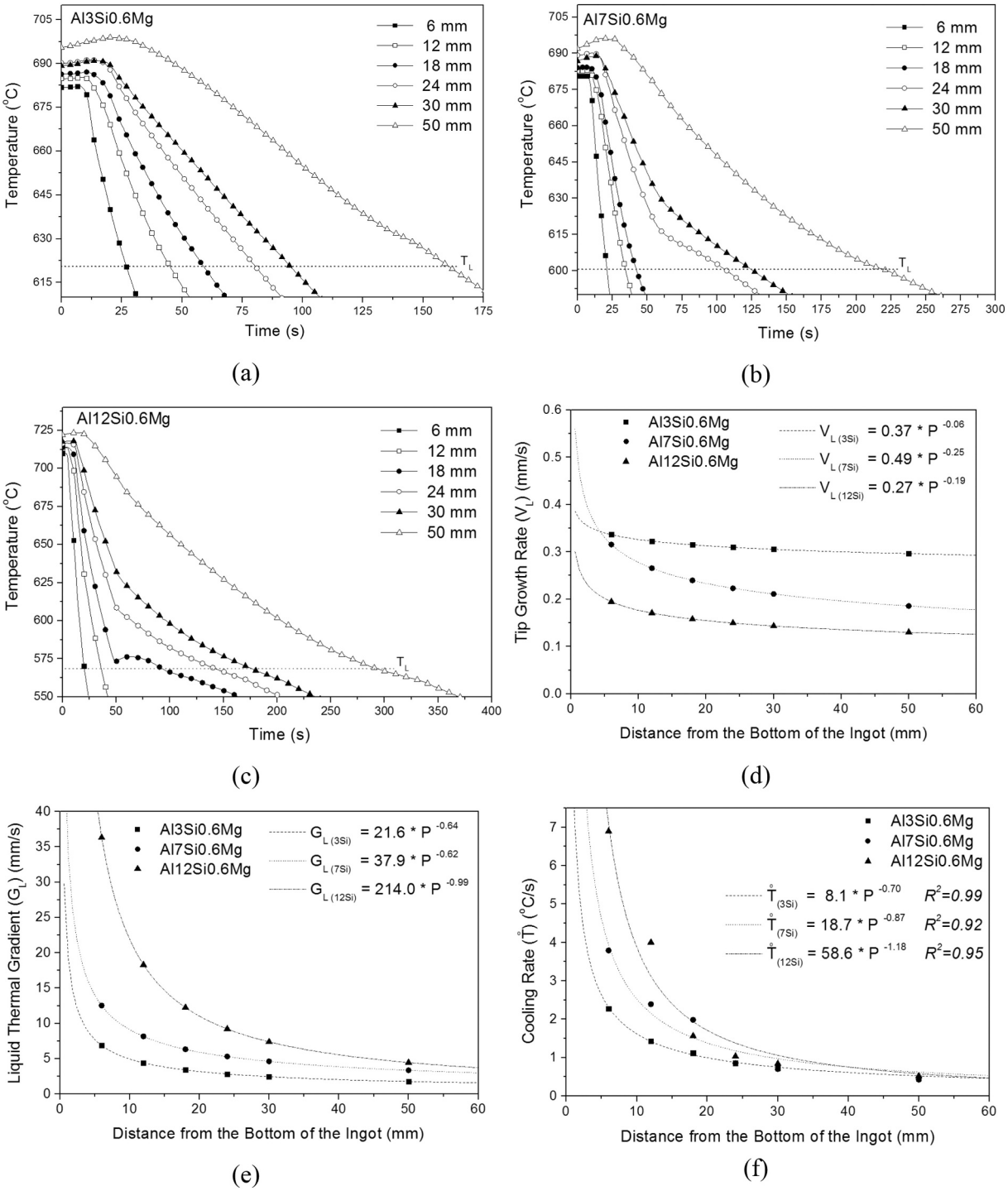

Fig. 4. Experimental cooling curves of the ingots: a) Al3Si0.6Mg, b) Al7Si0.6Mg, c) Al12Si0.6Mg, d) tip growth rate, e) liquid thermal gradient, f) cooling rate as a function of position.

the cutting tool. These results are in agreement with those reported by Barzani et al. [56] who observed that the presence of hard phases amplifies chip breakability and reduces chip adhesion. Demir and Gunduz [57] also stated that higher hardness facilitates material removal during machining in aging heat-treated alloys, preventing build-up edge formation.

In order to analyze the combined behavior of cutting force (*Fc*) and hardness, Fig. 10a to c show the resulting correlations for the different regions along the length of the as-cast ingots and the obtained experimental laws. The expressions for the secondary dendrite arm spacing were incorporated into the cutting force model, in order to derive general expressions that correlate λ_2 with *Fc* for the investigated as-cast alloys (Eqs. (1a) to (3c)).

Al3Si0.6Mg

$$F_{C(0-20\ \mathrm{mm})} = 55.06^{*}\left[48.7 + 42.1^{*}(\lambda_2)^{-0.5}\right] - 2977 \quad (1a)$$

$$F_{C(20-40\ \mathrm{mm})} = 63.46^{*}\left[48.7 + 42.1^{*}(\lambda_2)^{-0.5}\right] - 3391 \quad (1b)$$

$$F_{C(40-60\ \mathrm{mm})} = 73.72^{*}\left[48.7 + 42.1^{*}(\lambda_2)^{-0.5}\right] - 3892 \quad (1c)$$

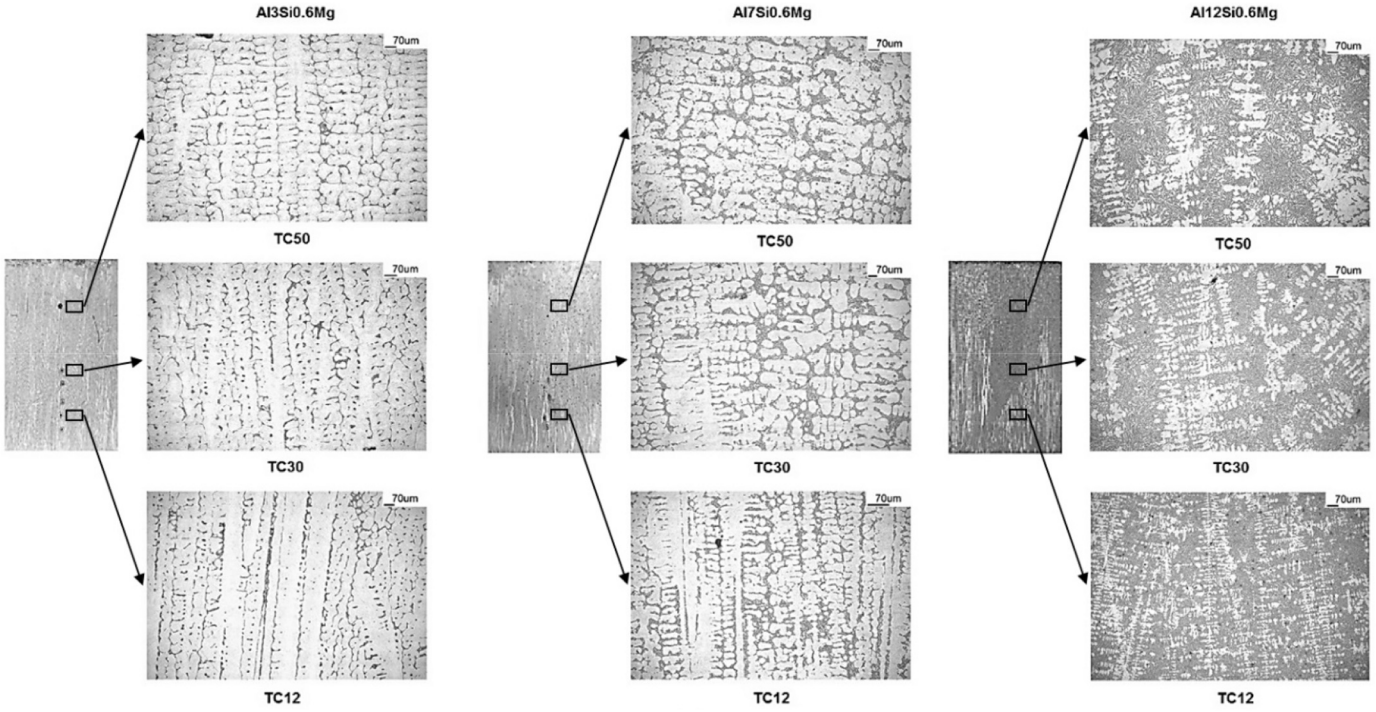

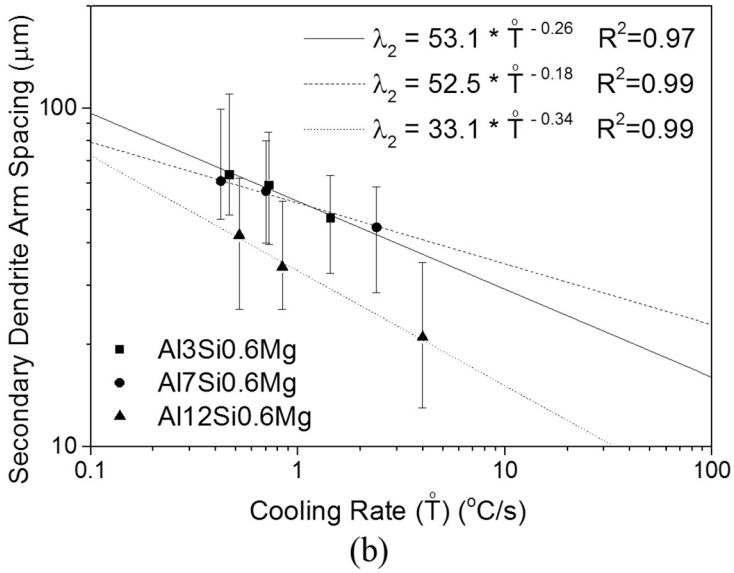

Fig. 5. a) Typical as-cast macrostructures and microstructures, b) secondary dendrite arm spacing as a function of cooling rate.

Al7Si0.6Mg

$$F_{C(0-20\ \mathrm{mm})} = 23.84^{*}\left[44.1 + 88.1^{*}(\lambda_2)^{-0.5}\right] - 1300 \quad (2a)$$

$$F_{C(20-40\ \mathrm{mm})} = 24.52^{*}\left[44.1 + 88.1^{*}(\lambda_2)^{-0.5}\right] - 1327 \quad (2b)$$

$$F_{C(40-60\ \mathrm{mm})} = 39.41^{*}\left[44.1 + 88.1^{*}(\lambda_2)^{-0.5}\right] - 2112 \quad (2c)$$

Al12Si0.6Mg

$$F_{C(0-20\ \mathrm{mm})} = 16.71^{*}\left[57.1 + 39.3^{*}(\lambda_2)^{-0.5}\right] - 1042 \quad (3a)$$

$$F_{C(20-40\ \mathrm{mm})} = 11.37^{*}\left[57.1 + 39.3^{*}(\lambda_2)^{-0.5}\right] - 678 \quad (3b)$$

$$F_{C(40-60\ \mathrm{mm})} = 14.63^{*}\left[57.1 + 39.3^{*}(\lambda_2)^{-0.5}\right] - 864 \quad (3c)$$

Direct comparison between experimental and calculated data using these equations is illustrated in Fig. 10d for the Al7Si0.6Mg alloy. As can be seen, relatively good agreement is observed, but the deviation increases for positions close to the bottom, where λ_2 shows the highest variation, or to the top of the ingot that is generally associated with a higher incidence of pores for directionally solidified Al-based alloys ingots [58].

4. Conclusions

The influence of as-cast and heat-treated microstructures and hardness on the machinability of Al-Si-Mg alloys with different Si content has

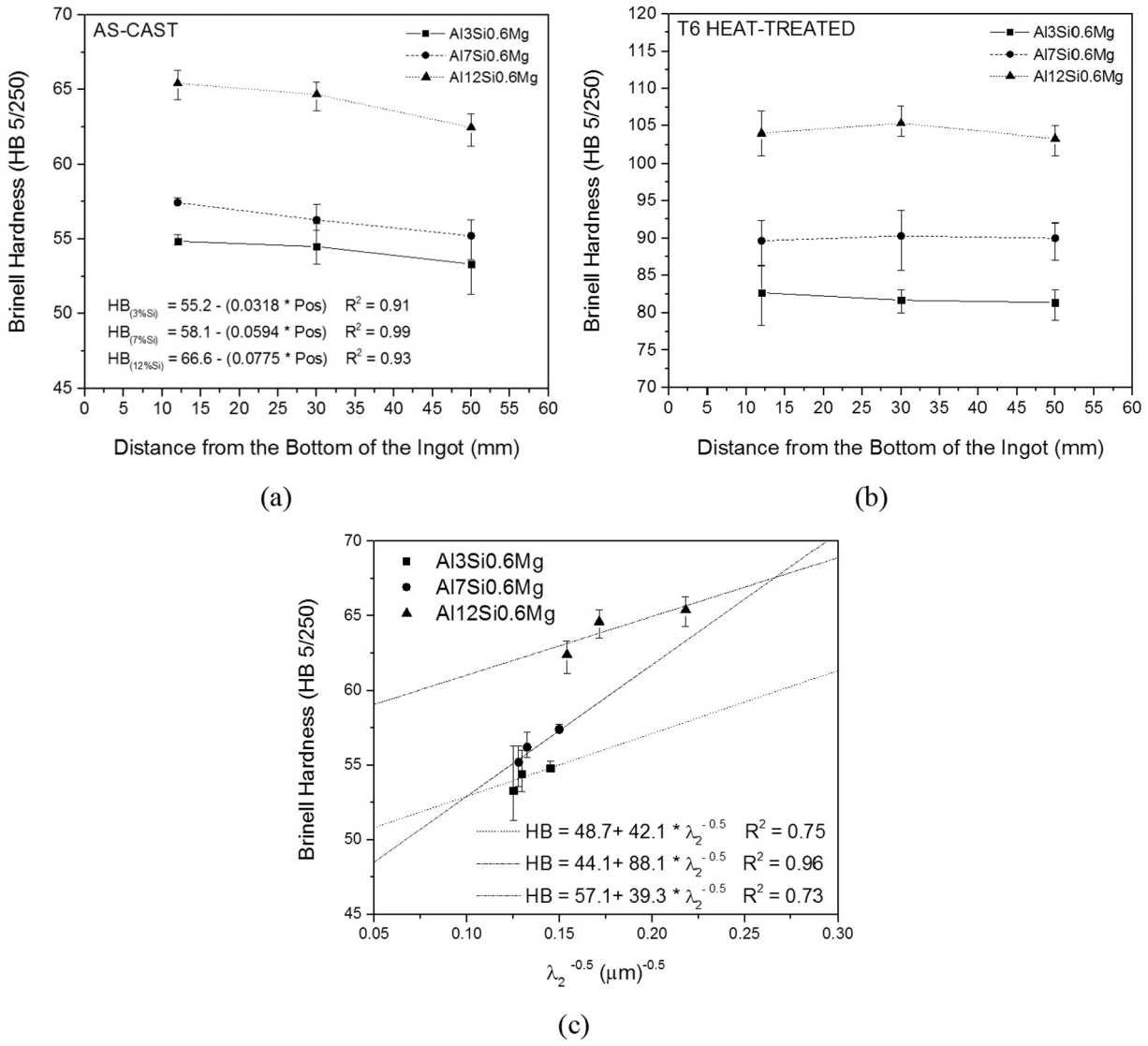

Fig. 6. Brinell hardness as a function of position along the length of the ingots: (a) as-cast, (b) heat-treated, (c) Hall-Petch type expressions HB vs $(\lambda_2)^{-0.5}$.

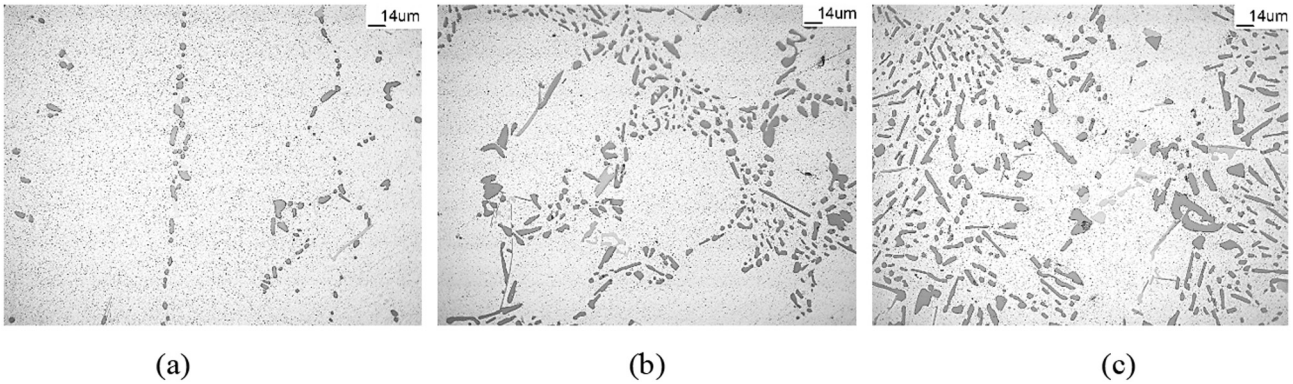

Fig. 7. Typical microstructures obtained for the alloys after heat treatment: a) Al3Si0.6Mg, b) Al7Si0.6Mg, c) Al12Si0.6Mg.

been investigated in this work. The following conclusions can be drawn from the results:

- Higher alloy Si content results in higher amount of the eutectic mixture in the microstructure, higher cooling rates during solidification, and consequently more refined λ_2;
- Hardness increases with the T6 heat treatment for all examined alloys, approximately 1.6× higher than that of the as-cast samples;

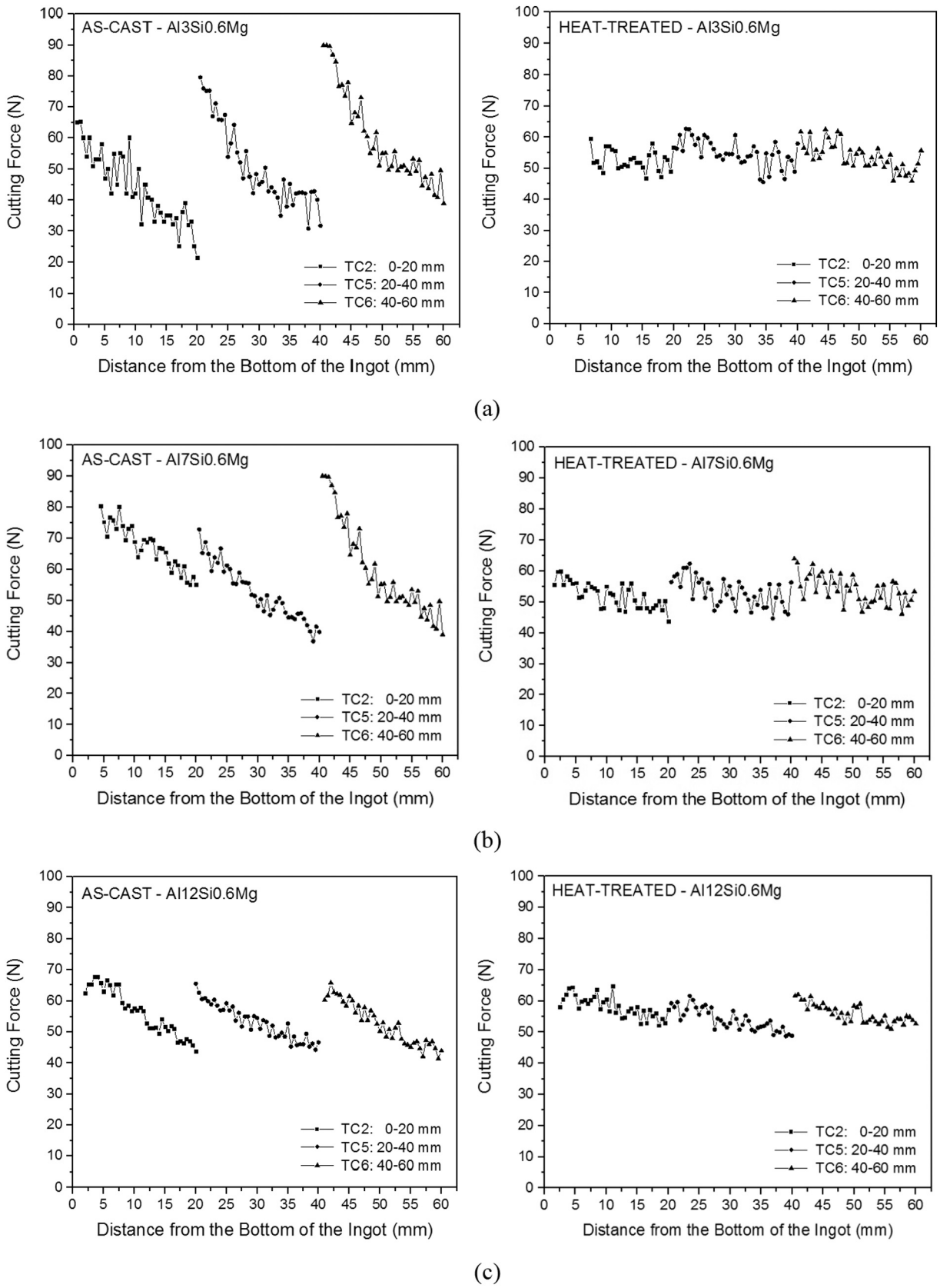

Fig. 8. Cutting force as a function of position along the length of the ingots for as-cast and heat-treated conditions: (a) Al3Si0.6Mg, (b) Al7Si0.6Mg, (c) Al12Si0.6Mg alloys.

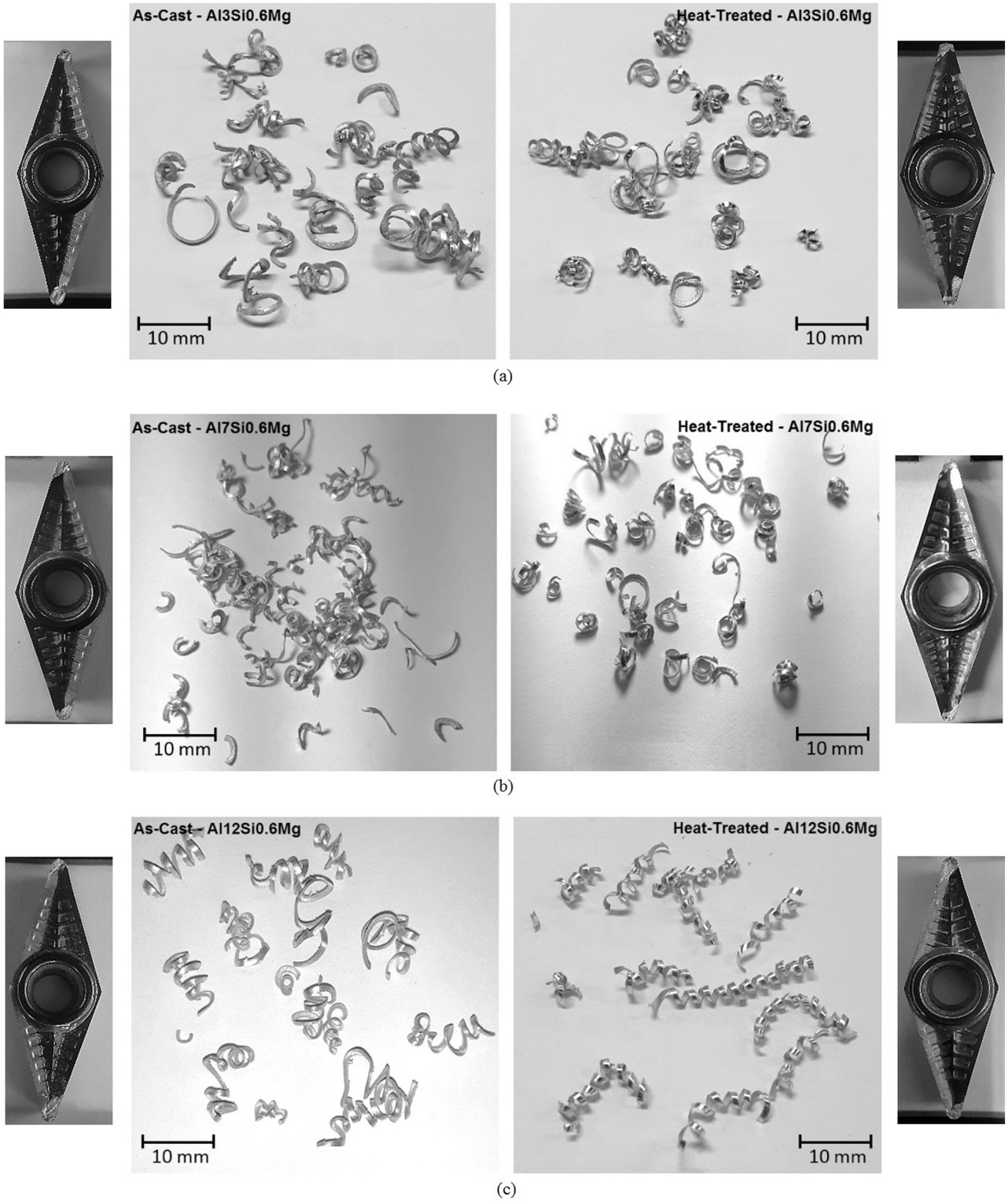

Fig. 9. Chip morphologies and cutting tools used for machining in the as-cast and heat-treated conditions: (a) Al3Si0.6Mg, (b) Al7Si0.6Mg, (c) Al12Si0.6Mg alloys.

- The increase in hardness is effective in improving the machining process by decreasing the cutting forces;
- Expressions for the secondary dendrite arm spacing were incorporated into the cutting force model, in order to derive general expressions that correlate λ_2 with *Fc* along the length of the investigated directionally solidified alloys castings;
- The results confirm that both microstructure and hardness play an important hole on the machinability behavior of as-cast and heat-treated alloys. However, despite the good agreement observed between the developed $Fc = f(\lambda_2)$ expressions and experimental results, further investigation is required to allow a better understanding of the set of additional metallurgical influencing mechanisms, such as

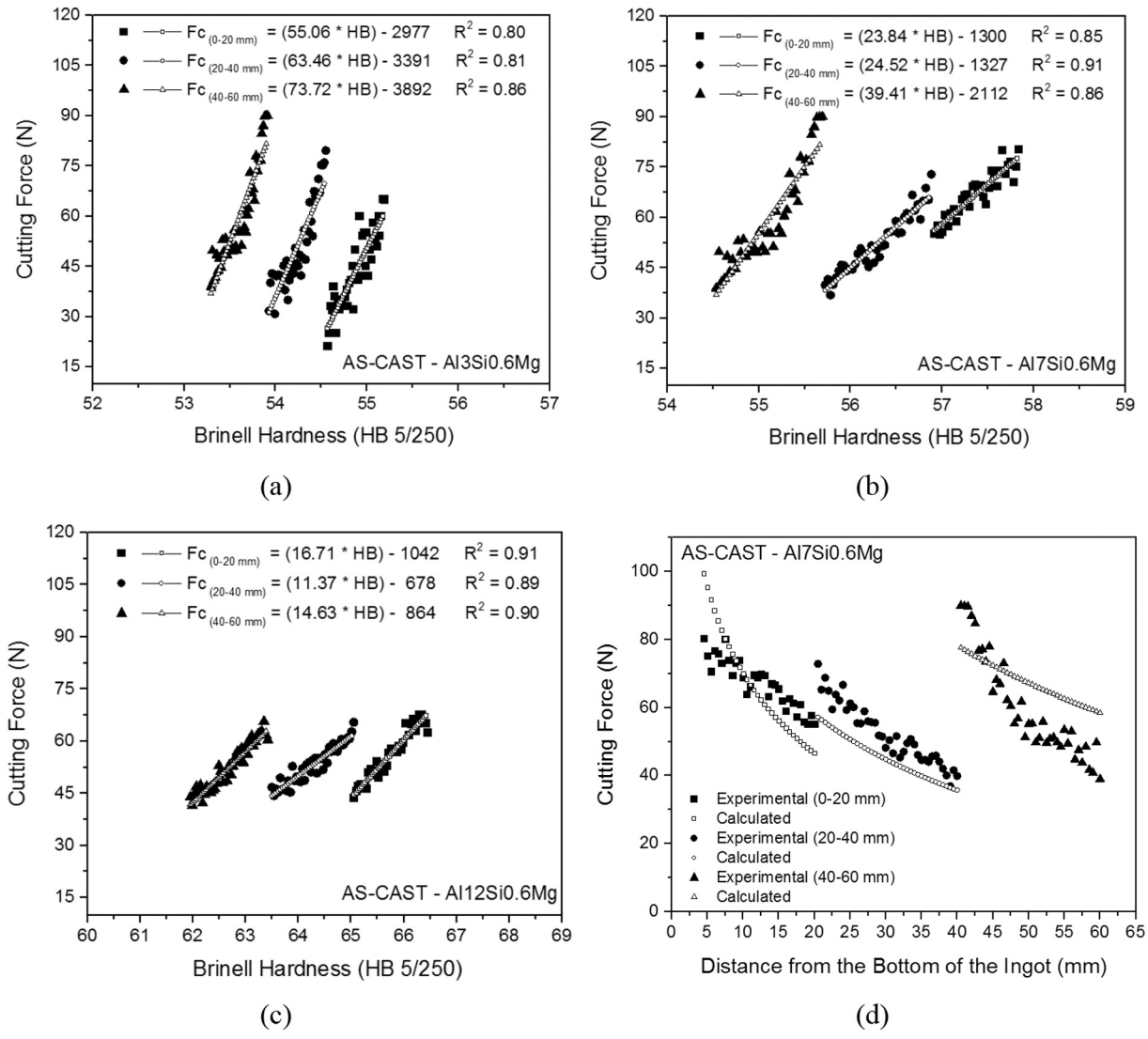

Fig. 10. Cutting force as a function of Brinell hardness along the regions of the ingots: (a) Al3Si0.6Mg, (b) Al7Si0.6Mg, (c) Al12Si0.6Mg.

the distribution of pores along the length of directionally solidified ingots.

Declaration of competing interest

The authors declare that they have no known competing financial interests or personal relationships that could have appeared to influence the work reported in this paper.

Acknowledgements

The authors acknowledge the support provided by CNPq (National Council for Scientific and Technological Development: grants: 403303/2016-8 and 303140/2020-8), FINEP (Financiadora de Estudos e Projetos: grant: 0082/16), FAPERGS (Fundação de Amparo à Pesquisa do Estado do Rio Grande do Sul) and PUCRS (Pontifícia Universidade Católica do Rio Grande do Sul). This study was financed in part by the Coordenação de Aperfeiçoamento de Pessoal de Nível Superior – Brasil (CAPES) – Finance Code 001.

References

[1] Davis JR. ASM specialty handbook: aluminum and aluminum alloys. Ohio: ASM International; 1993.
[2] Totten GE, MacKenzie DS. Handbook of aluminum. v. 2: alloy production and materials manufacturing. Boca Raton: Taylor and Francis Group; 2003.
[3] Zolotorevsky VS, Belov NA, Glazoff MV. Casting aluminum alloys. v. 12. Amsterdam: Elsevier; 2007.
[4] ASM handbook, castings. v. 15. Ohio: ASM International; 2002.
[5] Kaiser MS, Sabbir SH, Kabir MS, Soummo MR, Al Nurb M. Study of mechanical and wear behaviour of hyper-eutectic Al-Si automotive alloy through Fe, Ni and Cr addition. Mater Res 2018;21-4:1–9.
[6] Sunil B, Rajeev VR, Jose S. A statistical study in the dry wear and friction characteristics of Al-12.6Si-3Cu-(2–2.6wt.%)Ni piston alloys. Mater Today Proc 2018;5:1131–7.
[7] Li Y, Yang Y, Wu Y, Wei Z, Liu X. Supportive strengthening role of cr-rich phase on Al–Si multicomponent piston alloy at elevated temperature. Mater Sci Eng A 2011; 528:4427–30.
[8] Shara SK, Czerwinski F, Kasprzak W, Friedman J, Chen DL. Ageing characteristics and high-temperature tensile properties of Al-si-cu-mg alloys with micro-additions of cr, ti, V and zr. Mater Sci Eng A 2016;652:353–64.
[9] Jung JG, Lee SH, Cho YH, Yoon WH, Ahn TY, Ahn YS, Lee JM. Effect of transition elements on the microstructures and tensile properties of Al-12Si alloy cast under ultrasonic melt treatment. J Alloys Compd 2017;712:277–87.
[10] Giovanni M, Warnett JM, Williams MA, Srirangam P. 3D imaging and quantification of porosity and intermetallic particles in strontium modified Al-si alloys. J Alloys Compd 2017;727:353–61.
[11] Ahmad R. The effect of chromium addition on fluidity, microstructure and mechanical properties of aluminum lm6 cast alloy. Int J Mater Sci Res 2018;1(1): 32–5.
[12] Gloria A, Montanari R, Richetta M, Varone A. Alloys for aeronautic applications: state of the art and perspectives. Metals 2019;9:662–88.
[13] Liu YL, Kang SB, Kim HW. The complex microstructures in an as-cast Al–Mg–Si alloy. Mater Lett 1999;41:267–72.

[14] Brito C, Reinhart G, Nguyen-Thi H, Mangelinck-Noël N, Cheung N, Spinelli JE, Garcia A. High cooling rate cells, dendrites, microstructural spacings and microhardness in a directionally solidified Al–Mg–Si alloy. J Alloys Compd 2015; 636:145–9.
[15] Verma A, Kumar S, Grant PS, O'Reilly KAQ. Influence of cooling rate on the fe intermetallic formation in an AA6063 Al alloy. J Alloys Compd 2013;555:274–82.
[16] Yildirim M, Ozyurek D. The effects of mg amount on the microstructure and mechanical properties of Al-si-mg alloys. Mater Des 2013;51:767–74.
[17] Pedersen L, Arnberg L. The effect of solution heat treatment and quenching rates on mechanical properties and microstructures in AlSiMg foundry alloys. Mater Metall Trans A 2001;32:525–32.
[18] Gopikrishna S, Binu CY. Study on effects of T6 heat treatment on grain refined A319 alloy with magnesium and strontium addition. Int J Theor Appl Res Mech Eng 2013;2–3:59–62.
[19] Kaleel AJ. Study the effect of solution treatment on mechanical properties of Al-7% Si-0.3%Mg alloy. Nat Appl Sci 2013;4–4:195–200.
[20] Kaygisiz Y, Marasli N. Microstructural, mechanical and electrical characterization of directionally solidified Al–Si–Mg eutectic alloy. J Alloys Compd 2015;618: 197–203.
[21] Brito C, Vida T, Freitas E, Cheung N, Spinelli JE, Garcia A. Cellular/dendritic arrays and intermetallic phases affecting corrosion and mechanical resistances of an Al-mg-si alloy. J Alloys Compd 2016;673:220–30.
[22] ASTM B 108. In: Standard specification for aluminum – alloy permanent mold castings. 100 Barr Harbor Drive, West Conshohocken, PA, United States: ASTM International; 2019. p. 1–22.
[23] Wang QG, Davidson CJ. Solidification and precipitation behaviour of Al-si-mg casting alloys. J Mater Sci 2001;36:739–50.
[24] Stanic D, Brodarac ZZ, Li L. Influence of copper addition in AlSi7MgCu alloy on microstructure development and tensile strength improvement. Metals 2020;10: 1623–39.
[25] Ebrahimi A, Moshksar MM. Evaluation of machinability in turning of microalloyed and quenched-tempered steels: tool wear, statistical analysis, chip morphology. J Mater Process Technol 2009;209:910–21.
[26] Filho AW, Souza BV, Santos CA. The influence of austempering conditions on the machinability of a ductile iron. Mater Manuf Process 2016;31:1836–43.
[27] Tanaka T, Akasawa T. Machinability of hypereutectic silicon-aluminum alloys. J Mater Eng Perform 1999;8–4:463–8.
[28] Struzikiewicz G, Zebala W, Slodki B. Cutting parameters selection for sintered alloy AlSi10Mg longitudinal turning. Measurement 2019;138:39–53.
[29] Soren TR, Kumar R, Panigrahi I, Sahoo AK, Panda A, Das RK. Machinability behavior of aluminium alloys: a brief study. Mater Today Proc 2019;18:5069–75.
[30] Santos Jr MC, Machado AR, Sales WF, Barrozo MAS, Ezugwu EO. Machining of aluminum alloys: a review. Int J Adv Manuf Technol 2016;86:3067–80.
[31] Froehlich AR, Jacques RC, Strohaecker TR, Mombru R. The correlation of machinability and microstrutural characteristics of different extruded aluminum alloys. J Mater Eng Perform 2007;16–6:784–91.
[32] C Veera Ajay V Vinoth . Optimization of process parameters in turning of aluminum alloy using response surface methodology. Mater Today Proc, doi: 10.1016/j.matpr.2020.03.236.
[33] Gonçalves RA, Silva MB, Costa ES. Statistical analysis of cutting forces and hole accuracy in reaming an Al–Si–Mg alloy (6351) with different copper contents. J Braz Soc Mech Sci Eng 2018;40–544:1–19.
[34] Akyüz B, Şenaysoy S. Effect of the aging process on mechanical properties and machinability in AA6013 aluminum alloys. Acad J 2015;10–2:71–8.
[35] Bayraktar S, Afyon F. Machinability properties of Al–7Si, Al–7Si–4Zn and Al–7Si–4Zn–3Cu alloys. J Braz Soc Mech Sci Eng 2020;42–187:1–12.
[36] Barzani MM, Farahany S, Yusof NM, Ourdjini A. The influence of bismuth, antimony, and strontium on microstructure, thermal, and machinability of aluminum-silicon alloy. Mater Manuf Process 2013;28:1184–90.
[37] Kishawy HA, Dumitrescu M, Eg NG, Elbestawi MA. Effect of coolant strategy on tool performance, chip morphology and surface quality during high-speed machining of A356 aluminum alloy. Int J Mach Tools Manuf 2005;45:219–27.
[38] Tash M, Samuel FH, Mucciardi F, Doty HW, Valtierra S. Effect of metallurgical parameters on the machinability of heat-treated 356 and 319 aluminum alloys. Mater Sci Eng A 2006;434:207–17.
[39] Ache CT, Lopes MM, Reis BP, Garcia A, Santos CA. Dendritic spacing/columnar grain diameter of Al–2Mg–Zn alloys affecting hardness, tensile properties, and dry sliding wear in the as-cast/heat-treated conditions. Adv Eng Mater 2020;1 (1901145):1–11.
[40] Ribeiro TM, Catellan E, Garcia A, Santos CA. The effects of cr addition on microstructure, hardness and tensile properties of as-cast Al–3.8wt.%Cu–(Cr) alloys. J Mater Res Technol 2020;9–3:6620–31.
[41] ASTM E 10. In: Standard test method for Brinell hardness of metallic materials. 100 Barr Harbor Drive, West Conshohocken, PA, United States: ASTM International; 2017. p. 1–9.
[42] Silva C, Soares T, Cheung N, Garcia A, Reis DAP, Brito C. Dendritic spacing and macrosegregation affecting microhardness of an Al-si-mg alloy solidified under unsteady state conditions. Mater Res 2020;22–1:1–12.
[43] Taylor JA. Iron-containing intermetallic phases in Al-si based casting alloys. Procedia Mater Sci 2012;1:19–33.
[44] Bidmeshki C, Abouei V, Saghafian H, Shabestari SG, Noghani MT. Effect of mn addition on fe-rich intermetallics morphology and dry sliding wear investigation of hypereutectic Al-17.5%Si alloys. J Mater Res Technol 2016;5–3:250–8.
[45] Zhu X, Yang H, Dong X, Ji S. The effects of varying mg and si levels on the microstructural inhomogeneity and eutectic Mg2Si morphology in die-cast Al–Mg–Si alloys. J Mater Sci 2019;54:5773–87.
[46] Lima JO, Barbosa CR, Magno IAB, Nascimento JM, Barros AS, Oliveira MC, Souza FA, Rocha OL. Microstructural evolution during unsteady-state horizontal solidification of Al-si-mg (356) alloy. Trans Nonferrous Metals Soc China 2018; 28–6:1073–83.
[47] Brito C, Costa TA, Vida TA, Bertelli F, Cheung N, Spinelli JE, Garcia A. Characterization of dendrite microstructure, intermetallic phases, and hardness of directionally solidified Al-mg and Al-mg-si alloys. Metall Mater Trans A 2015;46–8: 3342–55.
[48] Chen R, Shi YF, Xu QY, Liu BC. Effect of cooling rate on solidification parameters and microstructure of Al-7Si-0.3Mg-0.15Fe alloy. Trans Nonferrous Metals Soc China 2014;24:1645–52.
[49] Yao JY, Taylor JA. Characterisation of intermetallic particles formed during solution treatment of an Al-7Si-0,4Mg-0,12Fe alloy. J Alloys Compd 2012;519: 60–6.
[50] Costa TA, Dias M, Gomes LG, Rocha OL, Garcia A. Effect of solution time in T6 heat treatment on microstructure and hardness of a directionally solidified Al-si-cu alloy. J Alloys Compd 2016;683:485–94.
[51] Magno IAB, Souza FVA, Barros AS, Costa MO, Nascimento JM, Costa TAPS, Rocha OFL. Effect of the T6 heat treatment on microhardness of a directionally solidified aluminum-based 319 alloy. Mater Res 2017;20–2:662–6.
[52] Souza FA, Costa MO, Magno IA, Nascimento JM, Silva AP, Costa TS, Rocha OL. Investigation on microstructural and microhardness evolution in as-cast and T6/ heat-treated samples of a horizontally solidified AlSiCu alloy. J Mater Res Technol 2019;8–5:5046–52.
[53] CAP Silva LRM Leal EC Guimarães PM Júnior AL Moreira OL Rocha CAP Silva Influence of thermal parameters, microstructure, and morphology of Si on machinability of an Al-7wt.%Si alloy directionally solidified. Adv Mater Sci Eng vol. 2018; Article ID 9512957, 12 pages.
[54] Kamiya M, Yakou T, Sasaki T, Nagatsuma Y. Effect of si content on turning machinability of Al-si binary alloy castings. Mater Trans 2008;49–3:587–92.
[55] Akyuz B. Effect of silicon content on machinability of Al-si alloys. Adv Sci Technol Res J 2016;10–31:51–7.
[56] Barzani MM, Sarhan AAD, Farahany S, Ramesh S, Maher I. Investigating the machinability of Al–Si–Cu cast alloy containing bismuth and antimony using coated carbide insert. Measurement 2015;62:170–8.
[57] Demir H, Gündüz S. The effects of aging on machinability of 6061 aluminium alloy. Mater Des 2009;30:1480–3.
[58] Boeira AP, Ferreira IL, Garcia A. Alloy composition and metal/mold heat transfer efficiency affecting inverse segregation and porosity of as-cast Al-cu alloys. Mater Des 2009;30:2090–8.